

Acoustic measurements of nucleus size distribution at the cavitation threshold

Lauren Mancia^{a,*}, Mauro Rodriguez^b, Jonathan Sukovich^c, Scott Haskell^c,
Zhen Xu^c, Eric Johnsen^a

^a*Department of Mechanical Engineering, University of Michigan, Ann Arbor, Michigan, USA*

^b*Division of Engineering and Applied Science, California Institute of Technology, Pasadena, California, USA*

^c*Department of Biomedical Engineering, University of Michigan, Ann Arbor, Michigan, USA*

Abstract

Understanding the acoustic cavitation threshold is essential for minimizing cavitation bioeffects in diagnostic ultrasound and for controlling cavitation-mediated tissue ablation in focused ultrasound procedures. The homogeneous cavitation threshold is an intrinsic material property of recognized importance to a variety of applications requiring cavitation control. However, acoustic measurements of the cavitation threshold in water differ from those predicted by classical nucleation theories. This persistent discrepancy is explained by combining novel methods for acoustically nucleating single bubbles at threshold with numerical modeling to obtain a nucleus size distribution consistent with first-principles estimates for ion-stabilized nuclei. We identify acoustic cavitation at threshold as a reproducible subtype of heterogeneous cavitation with a characteristic nucleus size distribution. Knowledge of the nucleus size distribution could inspire new approaches for achieving cavitation control in water, tissue, and a variety of other media.

Keywords: Cavitation, Nucleation, Intrinsic threshold, Bubble dynamics, Histotripsy, Focused ultrasound

*Corresponding Author: Lauren Mancia, lamanca@umich.edu

Introduction

Understanding the acoustic cavitation threshold is essential for the mitigation and control of cavitation bioeffects in diagnostic ultrasound (Church, 2002) and for cavitation control in therapeutic ultrasound procedures (Bader et al., 2019). Homogeneous cavitation occurs when a medium spontaneously ruptures under a tensile (negative) pressure exceeding its tensile strength (Leighton, 2012). Acoustic measurements of the homogeneous cavitation threshold in water range from -21 to -30 MPa at room temperature (Herbert et al., 2006; Davitt et al., 2010; Greenspan and Tschiegg, 1982; Bader et al., 2019), which are of significantly smaller magnitude than values predicted by classical nucleation theory (Debenedetti, 1996) and measured using microfluidic techniques (Ando et al., 2012). Self-ionization of water is a proposed source of ion impurities that destabilize water to cavitation (Davitt et al., 2010). Alternatively, these ions could stabilize preexisting nanoscale gas bubbles against dissolution (Akulichev, 1966) producing *bubbstons* (Bunkin and Bunkin, 1992; Sankin and Teslenko, 2003). Ion stabilization likely explains the observed longevity of bulk nanobubbles (Nirmalkar et al., 2018b,a; Fang et al., 2018; Zhu et al., 2016; Uchida et al., 2016) and suggests that acoustic methods could be measuring the onset of heterogeneous cavitation in a subpopulation of ion-stabilized, nanoscale nuclei rather than a genuine homogeneous threshold (Maxwell et al., 2013; Sankin and Teslenko, 2003). Nevertheless, the reproducibility of acoustic threshold measurements in water of variable purity implies that this subpopulation of nuclei is highly consistent (Maxwell et al., 2013; Borkent et al., 2007; Ando et al., 2012), *ubiquitous* in water (Azouzi et al., 2013; Davitt et al., 2010), and *intrinsic* to water and water-based tissues (Bader et al., 2019; Bunkin and Bunkin, 1992). Despite such robust experimental evidence of their existence, these nuclei remain poorly characterized.

Attempts to use fundamental thermodynamics (Bunkin and Bunkin, 1992) or nucleation theories to predict a critical or lower-bound cavitation nucleus size at a given temperature (Davitt et al., 2010; Azouzi et al., 2013) provide limited information about the distribution of nuclei in more practical settings, and failure to account for nucleus size variation within a cloud of acoustically-generated bubbles risks neglecting important physics (Wang, 1999). Prior work in heterogeneous cavitation suggests that nucleus sizes follow a lognormal (Ben-Yosef et al., 1975; Ando et al., 2011) or Weibull (Wienken et al., 2006) distribution, but it is not clear that these

distributions are applicable to nanoscale nuclei present at threshold. While it is possible to measure the size distributions and other characteristics of nanobubbles (Nirmalkar et al., 2018b,a; Fang et al., 2018; Zhu et al., 2016; Uchida et al., 2016; Bunkin et al., 2014, 2016; Jin et al., 2007), such studies involve methods that nucleate multiple bubbles simultaneously in water that often contains added ions (Zhu et al., 2016; Uchida et al., 2016; Bunkin et al., 2014, 2016; Jin et al., 2007). Though they are likely stabilized by similar physics (Akulichev, 1966), these nanobubbles are not necessarily representative of the hypothesized nanoscale nuclei present at the acoustic cavitation threshold in deionized water. Moreover, nanoparticle tracking analysis techniques considered most accurate for measuring nanobubble size distributions (Nirmalkar et al., 2018b) have detection limits in the tens of nanometers (Filipe et al., 2010)—larger than estimated sizes for acoustic threshold nuclei (Maxwell et al., 2013; Bader et al., 2019) or for preexisting bubbles in very dilute solutions (Bunkin and Bunkin, 1992). Finally, previous acoustic methods used to infer threshold nucleus sizes for water and other liquids have also been limited by an inability to track individual bubbles from their points of inception (Maxwell et al., 2013; Sankin and Teslenko, 2003). An alternative method adapts homogeneous nucleation theory to the study of acoustic cavitation in water and tissue (Church, 2002, 1993). This work assumed spontaneous generation of gas bubbles under energetically-favorable conditions and was used to estimate critical nucleus sizes for given sonication conditions. However, all of these methods are limited to inferring a mean or critical nucleus size that gives rise to a single cavitation event at a measured threshold pressure. To date, no study has both distinguished acoustic cavitation at threshold as a highly reproducible subtype of heterogeneous cavitation and provided measured cavitation statistics for the distribution of preexisting nuclei this implies.

Macroscopic cavitation activity in a variety of disciplines is likely affected by such a nucleus size distribution. The nuclei population is known to determine the onset of ultrasound-induced cavitation in water (Brotchie et al., 2009; Bader et al., 2019) and tissue (Maxwell et al., 2013; Vlasisavljevich et al., 2016, 2014, 2015) in biomedical ultrasound. The characteristics of intrinsic nuclei are of particular interest to histotripsy, a non-thermal focused ultrasound procedure that uses controlled cavitation to homogenize soft tissue into acellular debris (Xu et al., 2005; Parsons et al., 2006) for a variety of proposed clinical applications (Khokhlova et al., 2015). Mechanical tissue fractionation in histotripsy requires the creation of a dense cloud of cavitation

bubbles at the treatment focus (Parsons et al., 2007; Xu et al., 2005). Given the stochastic nature of cavitation, understanding the conditions required for bubble cloud generation and maintenance are important for treatment monitoring and planning (Bader et al., 2019). Furthermore, an understanding of the nuclei population in the relatively controlled setting of histotripsy treatments provides useful insight into nucleation in other settings. For example, cavitation inception in blast traumatic brain injuries (Salzar et al., 2017) and hydrodynamic applications (Chatterjee and Arakeri, 1997) is also thought to involve preexisting nuclei. Moreover, assumptions about the characteristics of initial cavities or defects in adhesives (Chikina and Gay, 2000), metals (Wilkerson and Ramesh, 2016), and amorphous solids (Singh et al., 2016; Guan et al., 2013) are needed to predict cavitation failure of these materials. Given the stochastic nature of cavitation phenomena, the ability to characterize and potentially control the nuclei population in a given medium would be useful to all of these applications (Brotchie et al., 2009; Maxwell et al., 2013; Chatterjee and Arakeri, 1997).

This study presents measurements of nanoscale cavitation nuclei in water, specifically, for the first time, a complete size distribution of nuclei induced to grow at the acoustic cavitation threshold. Our measurements are made by combining a unique ultrasound system capable of producing a single cavitation bubble at threshold (Wilson et al., 2019) with validated numerical modeling (Estrada et al., 2018).

Methods

Single-Bubble Experiments

Single-bubble experiments were previously performed in a study comparing laser- to ultrasound-generated cavitation in water and gels (Wilson et al., 2019), and we leverage the data sets from the water experiments. In brief, water is deionized to a resistivity of 18 megaohms, filtered to 2 μm , and degassed to 4 kPa. Experiments use a spherical acoustic array containing 16 focused transducer elements with a central frequency of 1 MHz that is capable of generating a single cavitation bubble with a well-characterized pressure waveform. Such control ensures that energy input to grow the bubble is known for a given nucleus size. Single bubbles are nucleated with a probability of 0.5 using a 1.5-cycle acoustic pulse which has a single rarefactional pressure half-cycle with an amplitude of -24 MPa. This value is consistent with measurements obtained by our group and others using variable

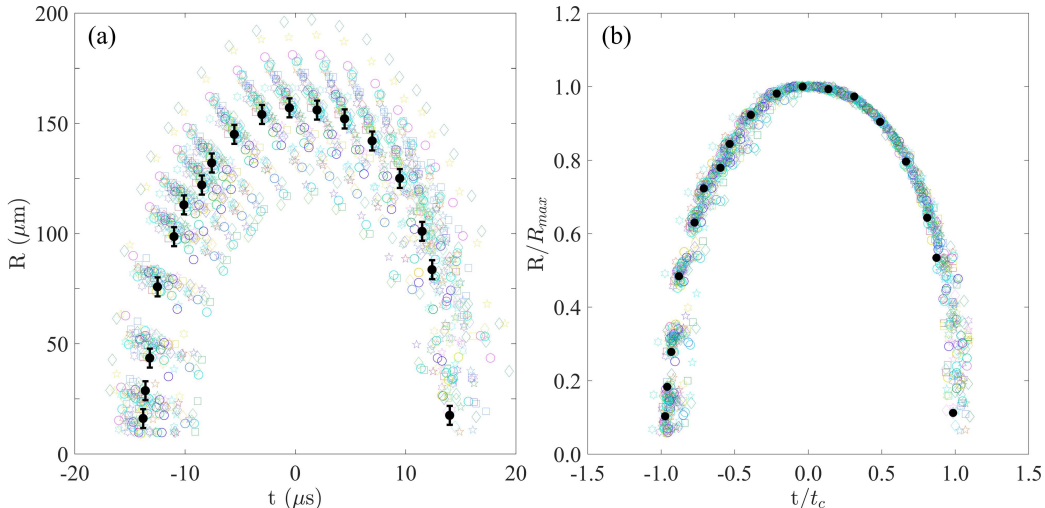


Figure 1: (a) Radius vs. time measurements from 88 experiments in water degassed to 4 kPa. Clustering of data sets is a consequence of aligning all data such that the maximum radii occur at $t = 0$. A single data set is shown in black with spatial resolution error bars. (b) Data sets scaled by maximum radius and collapse time.

acoustic waveforms and water purity (Herbert et al., 2006; Maxwell et al., 2013; Vlaisavljevich et al., 2016). Images of the bubbles through a single cycle of growth and collapse are obtained using a high-speed camera with a multi-flash-per-camera-exposure technique (Sukovich et al., 2020). This technique generates images of nested, concentric bubbles which are differentiated using brightness thresholding and edge detection. Bubble radii are measured at individual flash points by applying a least squares circle fit to their detected boundaries. For all experiments, the magnitudes of the spatial and temporal resolution uncertainties are $4.3 \mu\text{m}$ and $\leq 1.25 \mu\text{s}$, respectively.

Aggregate radius vs. time data sets for 88 acoustically-nucleated single-bubble experiments in water degassed to 4 are shown in Figure 1(a). Although all of the bubbles represented in the curves in Fig. 1(a) were generated under equivalent experimental conditions, significant differences between individual experiments are evident. Black points are a single representative data set, and error bars correspond to uncertainty associated with limitations in spatial resolution. Given that most of the other data sets fall outside of these error bars, it can be concluded that error associated with limitations in spatial resolution does not explain the data spread. Figure 1(b) shows

that the data sets collapse when scaled by the measured maximum radius and collapse time, $t_c = 0.92R_{max}\sqrt{\rho_\infty/P_\infty}$, where R_{max} is the maximum bubble radius of a given data set, ρ_∞ is liquid density, and P_∞ is the far-field liquid pressure (both constants given in Table 1). Thus, all experiments are governed by the same physics with exceedingly small uncertainty once appropriate scaling addresses uncertainties in initial conditions. In particular, the energy delivered by the ultrasound pulse to the nucleus grows the bubble as the bubble expands to maximum radius against its surroundings. That initial energy is proportional to the nucleus volume and ultrasound pressure amplitude. Given the negligible error in pressure amplitude measurement and its consistency with previous studies (Davitt et al., 2010), we submit that the data spread is due to different nanoscale nucleus sizes corresponding to each experiment. Validated numerical methods can then be used in combination with experimental data to infer these unknown nucleus sizes.

Theoretical Model

We simulate the dynamics of a single spherical, homobaric air bubble in water. To account for near-field compressibility effects, radial bubble dynamics are described by the Keller–Miksis equation (Keller and Miksis, 1980):

$$\begin{aligned} \left(1 - \frac{\dot{R}}{c_\infty}\right) R\ddot{R} + \frac{3}{2} \left(1 - \frac{\dot{R}}{3c_\infty}\right) \dot{R}^2 = \\ \frac{1}{\rho_\infty} \left(1 + \frac{\dot{R}}{c_\infty} + \frac{R}{c_\infty} \frac{d}{dt}\right) \left[p_B - \right. \\ \left. \left(p_\infty + p_f \left(t + \frac{R}{c_\infty} \right) \right) - \frac{2\sigma}{R} + J \right], \end{aligned} \quad (1)$$

where R is the bubble radius, c_∞ and ρ_∞ are the constant sound speed and density of the medium, respectively. The surface tension, σ and viscosity, μ are constants for water at 25 °C. These parameters and others that remain constant for all simulations are given in Table 1.

Heat transfer effects are considered by solving for temperature fields inside and outside of the bubble. The time derivative of the internal bubble pressure, $p_B(t)$ couples the Keller–Miksis equation (Eq. 1) to the energy equation for air inside the bubble:

$$\dot{p}_B = \frac{3}{R} \left((\kappa - 1)K \frac{\partial T}{\partial r} \Big|_R - \kappa p_B \dot{R} \right) \quad (2)$$

$$\begin{aligned} \frac{\kappa}{\kappa - 1} \frac{p_B}{T} \left[\frac{\partial T}{\partial t} + \frac{1}{\kappa p_B} \left((\kappa - 1)K \frac{\partial T}{\partial r} - \frac{r \dot{p}_B}{3} \right) \frac{\partial T}{\partial r} \right] \\ = \dot{p}_B + \frac{1}{r^2} \frac{\partial}{\partial r} \left(r^2 K \frac{\partial T}{\partial r} \right), \end{aligned} \quad (3)$$

where $T(r, t)$ is the temperature field of air inside the bubble, which has a ratio of specific heats κ . The air has a thermal conductivity given by $K = K_A T + K_B$, where constants K_A and K_B were determined empirically for air (Prosperetti et al., 1988). The initial pressure inside the bubble is $p_B(0) = p_\infty + 2S/R$. A boundary condition is prescribed for the center of the bubble: $\nabla T = 0$ at $r = 0$. The bubble wall boundary condition is simplified to $T(R) = T_\infty$ under the assumption that the water remains at its constant ambient temperature through the single cycle of bubble growth and collapse considered in each experiment (Prosperetti, 1991; Estrada et al., 2018).

The far-field pressure is the sum of the ambient pressure, p_∞ and time-varying incident pulse, $p_f(t)$:

$$p_f(t) = \begin{cases} p_A \left(\frac{1 + \cos[\omega(t - \delta)]}{2} \right)^n, & |t - \delta| \leq \frac{\pi}{\omega}, \\ 0, & |t - \delta| > \frac{\pi}{\omega}. \end{cases} \quad (4)$$

The pressure amplitude, $p_A = -24$ MPa and frequency, $f = 1$ MHz ($\omega = 2\pi f$) are approximated from experimental waveform measurements while the time delay, $\delta = 5 \mu s$ and fitting parameter, n are chosen as in previous studies (Vlaisavljevich et al., 2014; Mancina et al., 2017). Based on the notion of a cavitation threshold, cavitation only occurs if a sufficiently large tension is applied. The experimental waveform consists of several cycles, and only the peak negative portion is beyond threshold. An analytic approximation of this peak negative pressure portion of a raw experimental waveform (Mancina et al., 2019) is valid in this near ideal case of inertial cavitation in which resonant frequency of the bubble is much less than the driving frequency of the waveform.

Table 1: Constant Parameters

Parameter	Value
p_A	-24 MPa
f	1 MHz
n	3.7
δ	5 μ s
S	72 mN/m
c_∞	1496 m/sec
ρ_∞	1000 kg/m ³
p_∞	101.325 kPa
T_∞	25 °C
κ	1.4
K_A	5.28×10^{-5} W/mK ²
K_B	1.165×10^{-2} W/mK

Problem Setup

The equations are nondimensionalized (Warnez and Johnsen, 2015) using the initial bubble radius, R_0 , water density, ρ_∞ , equilibrium pressure of the bubble contents, $p_0 = p_\infty + 2\sigma/R$, and far-field temperature, T_∞ to define a characteristic speed, $u_c = \sqrt{p_0/\rho_\infty}$ and dimensionless parameters: Reynolds number, $\text{Re} = \rho_\infty u_c R_0/\mu$, Weber number, $\text{We} = p_0 R_0/2S$, dimensionless sound speed, $C = c_\infty/u_c$, and $\chi = T_\infty K_M/p_0 R_0 u_c$. A variable-step, variable-order solver based on numerical differentiation formulas (MATLAB *ode15s*) is used for numerical time marching (Shampine and Reichelt, 1997; Shampine et al., 1999). Equations are integrated over a dimensional time span of $t = [0, 50]$ in microseconds; results are then time-shifted so that the maximum bubble radius occurs at $t = 0$. Using numerical methods described by (Warnez and Johnsen, 2015), the spatial derivatives in the energy equation are discretized on a mesh of $N_s + 1$ points in r -space (Prosperetti et al., 1988) inside the bubble and computed using a spectral collocation method (Warnez and Johnsen, 2015). Results are sufficiently converged when simulations use $N_s = 30$ points inside the bubble. A more detailed treatment of the derivation and numerical implementation of this model can be found in the literature (Prosperetti et al., 1988; Kamath et al., 1993; Barajas and Johnsen, 2017; Warnez and Johnsen, 2015).

Results

To construct the nucleus size distribution, we hypothesize that cavitation nuclei exist as stabilized nanobubbles (Maxwell et al., 2013; Sankin and Teslenko, 2003) and seek to determine the minimum nucleus size, R_0^* required for cavitation growth at a given threshold pressure. Based on past work on the acoustic cavitation threshold (Maxwell et al., 2013; Vlasisavljevich et al., 2015, 2016), the threshold pressure is fixed at its measured value of -24 MPa for all simulations. Figure 2(a) shows the simulation maximum bubble radius as a function of nucleus size under this tensile pressure. Bubble growth is negligible until a minimum nucleus size of $R_0^* = 2.32$ nm is reached. Because the time of the tensile pulse is much longer than the timescale of the bubble, the quasistatic assumption holds, and the minimum nucleus size can be calculated from the Blake threshold (Leighton, 2012). The minimum pressure amplitude needed to cause explosive growth of a bubble with initial radius R_0 is given by:

$$P_B = P_\infty + \frac{8\sigma}{9} \sqrt{\frac{3\sigma}{2(P_\infty + 2\sigma/R_0)R_0^3}}, \quad (5)$$

where P_B is the Blake threshold, $P_\infty = 101.325$ kPa is the ambient pressure of the surrounding fluid, and $\sigma = 0.072$ N/m is the surface tension of water at 25°C . Assuming $2\sigma/R_0 \gg P_0$ for these nanoscale nuclei gives rise to a simplified expression for R_0 :

$$R_0 = \frac{4\sigma}{3\sqrt{3}} \left(\frac{1}{P_B - P_\infty} \right). \quad (6)$$

In the present case, the Blake threshold pressure is equivalent to the measured threshold pressure: $P_B = 24$ MPa. Substituting the other physical constants into Eq. 6 gives $R_0 = 2.32$ nm $= R_0^*$, which is the minimum bubble radius that will grow when exposed to the measured Blake threshold pressure (Walton and Reynolds, 1984). For comparison, previous studies estimate the minimum radii of stabilized nanoscale nuclei to be approximately 2.0 nm (Bunkin and Bunkin, 1992) from first principles and 2.5 nm (Maxwell et al., 2013) from bubble dynamics simulations. In contrast, critical nucleus volumes obtained using homogeneous nucleation theories correspond to radii of 1.3 nm (Davitt et al., 2010) and 0.88 nm (Azouzi et al., 2013) at 300 K.

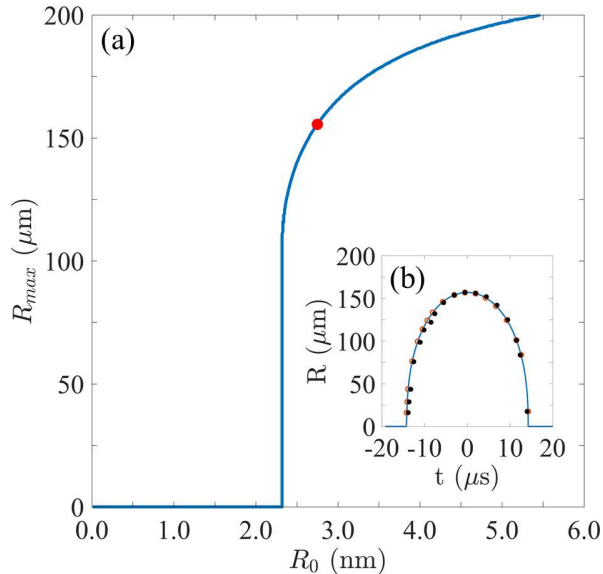


Figure 2: (a) Simulation R_{max} vs. nucleus size. (b) A representative data set in black. The simulation (blue trace) initialized with R_0 indicated by solid red point in (a) optimizes the normalized rms error between experiment and simulation nearest neighbors (red open points).

The complete nucleus size distribution is created by varying the R_0 used to initialize simulations over a range of 2.32 – 6.00 nm for each experimental data set. A nearest neighbors algorithm with a standardized Euclidean distance metric is then used to identify simulation points closest to experimental data points. The nucleus distribution consists of R_0 values that optimize the normalized root-mean-squared (rms) error between individual data points of a given experimental realization and their simulation nearest neighbors. The average normalized rms error for these data sets is 0.98 (with 1.00 implying a perfect fit). Figure 2(b) shows the representative data set from Figure 1. The simulation initialized with $R_0 = 2.78$ nm (indicated by the red point in Figure 2(a)) optimizes the normalized rms error between the experimental data (black points) and the nearest neighbors on the simulation trace (red open points). In this case, the normalized rms error is 0.98, which is equivalent to the mean error for all data sets. This procedure is followed for each data set to obtain R_0 values optimizing the normalized rms error.

Simulations initialized with different nucleus sizes effectively bound the experimental data sets as shown in Figure 3. Aggregate experimental data

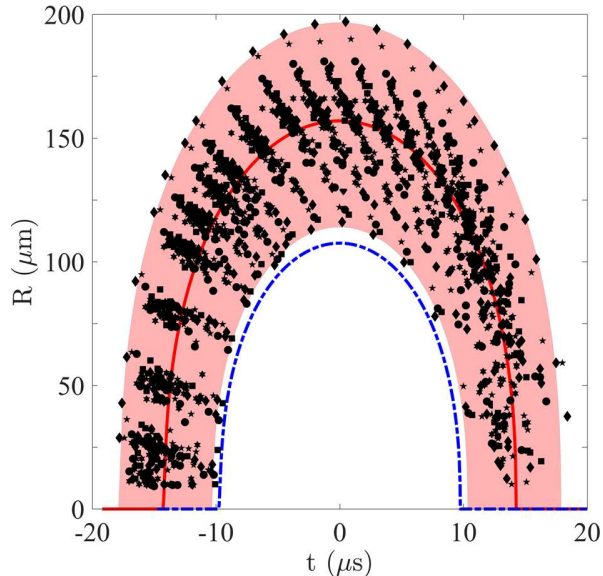


Figure 3: Experimental data from Fig. 1. Shaded region is bounded by simulations initialized with the smallest and largest nuclei. The dark red trace is the simulation corresponding to the mean nucleus size. The dashed blue trace is the simulation initialized with R_0^* .

from Figure 1 are shown in black, and the shaded region is bounded by simulations initialized with the smallest nucleus size, $R_0 = 2.33$ nm and the largest nucleus size, $R_0 = 4.99$ nm that optimize the normalized rms error. The dark red trace is the simulation initialized with the mean nucleus size of 2.88 nm, and the blue dashed trace is the simulation initialized with the predetermined, lower-bound nucleus, $R_0^* = 2.32$ nm. The nucleus size distribution is best approximated by a lognormal probability distribution function (pdf), outlined in red in Figure 4, which has $\sigma = 0.11$ and $\mu = 1.0$. This finding is consistent with previous use of a lognormal distribution to model equilibrium bubble sizes for polydisperse flow based on measured bubble populations in a water tunnel and ocean water (Ben-Yosef et al., 1975; Ando et al., 2011).

Discussion

The nucleus size distribution is consistent with previous studies which estimated the sizes of ion-stabilized nuclei to be between 2 and 4 nm (Sankin and Teslenko,

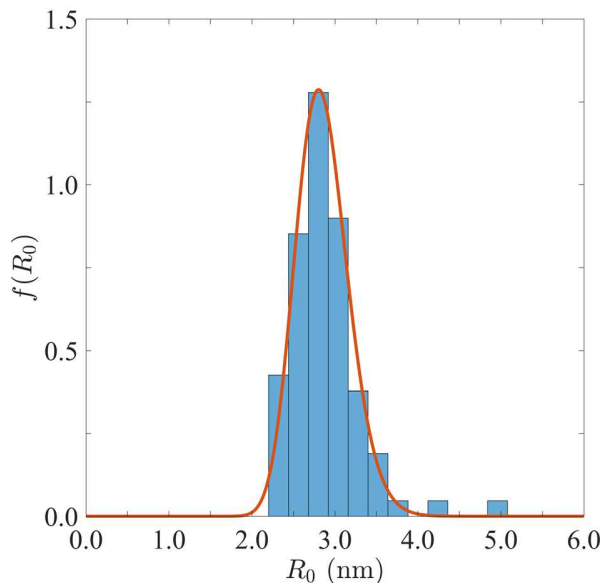


Figure 4: Nucleus size distribution fitted to lognormal pdf (red).

2003; Bunkin and Bunkin, 1992), and supports the hypothesis that hydroxium ions (e.g. those produced during self-ionization of water) are the ubiquitous impurity responsible for the discrepancy between acoustically-measured and theoretical homogeneous cavitation thresholds (Davitt et al., 2010). The lognormal pdf parallels size distributions measured for larger cavitation bubbles in settings of heterogeneous cavitation (Ben-Yosef et al., 1975; Ando et al., 2011), and nuclei measured in this study are at least 1 nm larger than critical nucleus sizes obtained using homogeneous nucleation theories at comparable pressure amplitudes. These findings suggest that acoustic methods, even in highly purified water, are measuring a threshold for heterogeneous rather than homogeneous cavitation. However, consistency in measurements (Herbert et al., 2006; Davitt et al., 2010; Greenspan and Tschiegg, 1982) distinguishes cavitation at the acoustic threshold as a reflection of the nuclei population intrinsic to that medium.

Despite significant differences in waveform and water quality used in previous experiments (Herbert et al., 2006; Maxwell et al., 2013), measured acoustic cavitation thresholds differ from each other and from ours by < 4 MPa. A previous study also notes that their threshold measurements are stable even to the deliberate introduction of impurities (Herbert et al., 2006).

However, there is evidence that gas concentration of the water could give rise to larger nuclei (Akulichev, 1966). To investigate this possibility, preliminary experiments were performed with water degassed to 40 kPa ($\sim 40\%$ oxygen saturation) instead of to the original 4 kPa ($\sim 4\%$ oxygen saturation) in our original experiments (Wilson et al., 2019). The higher gas content had a negligible effect on the measured acoustic cavitation threshold of -24 MPa. From 28 single-bubble experimental data sets, we inferred a mean nucleus size of 3.60 nm with nucleus sizes ranging from 2.64 nm to 5.78 nm. Although the newly measured nuclei are slightly larger, as expected from the arguments presented in (Akulichev, 1966), the mean nucleus sizes agree to within < 1 nm despite the ten-fold difference in gas content of the water. These results support previous findings that both the acoustic cavitation threshold is relatively stable to changes in water purity. Future work will further investigate the role of gas content, pH, and additive ions on the acoustic cavitation threshold in water and its associated nucleus size distribution.

Our method for determining the nucleus size distribution infers quantities well below the resolution limits of experiments, but our theory could be strengthened by greater consideration of nanoscale physics. For example, ion interactions could affect the earliest stages of bubble growth when nucleus sizes are nanoscopic. Additionally, nucleation phenomena are highly dependent on surface tension (Church, 2002), and the effective surface tension experienced by a nanoscale nucleus differs from that of the bulk medium (Azouzi et al., 2013). Investigation of these effects will be the subject of future work, with molecular dynamics simulations offering the most robust approach. Finally, our work has focused on water given its well-characterized physical properties and an acoustic cavitation threshold that is comparable to that of water-based soft tissues (Bader et al., 2019). In future work, we intend to extend these results to other liquids and viscoelastic media exhibiting thresholds outside of the typical range for water and water-based tissues (Maxwell et al., 2013).

Conclusions

In summary, this work presents a new approach for using single-bubble experiments and numerical simulations to measure the size distribution of nanoscale cavitation nuclei present at the acoustic cavitation threshold. Recognizing that the leading-order experimental uncertainty lies in the initial nuclei population, the inverse problem for the nucleus size distribution is

solved with a single-bubble numerical model. The nucleus size distribution obeys a lognormal pdf ranging from 2.33 to 4.99 nm with a mean of 2.88 nm. Although water is the only medium considered in this study, the methods presented here could be readily extended to predict the intrinsic nucleus size distributions characteristic of other liquids and tissue-like media, thus offering a new avenue for achieving cavitation control in biomedical ultrasound and a variety of other applications.

Acknowledgements

The authors wish to thank Prof. J. Brian Fowlkes for helpful discussions. This work was supported by ONR Grant No. N00014-18-1-2625 (under Dr. Timothy Bentley).

References

- Akulichev V. Hydration of ions and the vacitation resistance of water. *Acoustical Physics*, 1966;12:144–150.
- Ando K, Colonius T, Brennen CE. Numerical simulation of shock propagation in a polydisperse bubbly liquid. *Int. J. Multiph. Flow*, 2011;37:596–608.
- Ando K, Liu AQ, Ohl CD. Homogeneous nucleation in water in microfluidic channels. *Phys. Rev. Lett.*, 2012;109:044501.
- Azouzi MEM, Ramboz C, Lenain JF, Caupin F. A coherent picture of water at extreme negative pressure. *Nat. Phys.*, 2013;9:38.
- Bader KB, Vlasisavljevich E, Maxwell AD. For whom the bubble grows: physical principles of bubble nucleation and dynamics in histotripsy ultrasound therapy. *Ultrasound Med. Biol.*, 2019.
- Barajas C, Johnsen E. The effects of heat and mass diffusion on freely oscillating bubbles in a viscoelastic, tissue-like medium. *J. Acoust. Soc. Am.*, 2017;141:908–918.
- Ben-Yosef N, Ginio O, Mahlab D, Weitz A. Bubble size distribution measurement by doppler velocimeter. *J. Appl. Phys.*, 1975;46:738–740.
- Borkent BM, Arora M, Ohl CD. Reproducible cavitation activity in water-particle suspensions. *J. Acoust. Soc. Am.*, 2007;121:1406–1412.
- Brotchie A, Grieser F, Ashokkumar M. Effect of power and frequency on bubble-size distributions in acoustic cavitation. *Phys. Rev. Letters*, 2009;102:084302.
- Bunkin N, Bunkin F. Bubbstons: stable microscopic gas bubbles in very dilute electrolytic solutions. *J. Exp. Theor. Phys.*, 1992;74:271–276.
- Bunkin NF, Shkirin AV, Burkhanov IS, Chaikov LL, Lomkova AK. Study of the nanobubble phase of aqueous nacl solutions by dynamic light scattering. *Quantum Electronics*, 2014;44:1022.

- Bunkin NF, Shkirin AV, Suyazov NV, Babenko VA, Sychev AA, Penkov NV, Belosludtsev KN, Gudkov SV. Formation and dynamics of ion-stabilized gas nanobubble phase in the bulk of aqueous nacl solutions. *J. Phys. Chem. B*, 2016;120:1291–1303.
- Chatterjee D, Arakeri VH. Towards the concept of hydrodynamic cavitation control. *J. Fluid Mech.*, 1997;332:377–394.
- Chikina I, Gay C. Cavitation in adhesives. *Phys. Rev. Letters*, 2000;85:4546.
- Church CC. An alternative to the mechanical index as a means of assessing the safety of exposures to diagnostic ultrasound. *The Journal of the Acoustical Society of America*, 1993;93:2348–2348.
- Church CC. Spontaneous homogeneous nucleation, inertial cavitation and the safety of diagnostic ultrasound. *Ultrasound in medicine & biology*, 2002;28:1349–1364.
- Davitt K, Arvengas A, Caupin F. Water at the cavitation limit: Density of the metastable liquid and size of the critical bubble. *EPL*, 2010;90:16002.
- Debenedetti PG. *Metastable liquids: concepts and principles*. Princeton University Press, 1996.
- Estrada JB, Barajas C, Henann DL, Johnsen E, Franck C. High strain-rate soft material characterization via inertial cavitation. *J. Mech. Phys. Solids*, 2018;112:291–317.
- Fang Z, Wang L, Wang X, Zhou L, Wang S, Zou Z, Tai R, Zhang L, Hu J. Formation and stability of surface/bulk nanobubbles produced by decompression at lower gas concentration. *J. Phys. Chem. C*, 2018;122:22418–22423.
- Filipe V, Hawe A, Jiskoot W. Critical evaluation of nanoparticle tracking analysis (nta) by nanosight for the measurement of nanoparticles and protein aggregates. *Pharm. Res.*, 2010;27:796–810.
- Greenspan M, Tschiegg CE. Radiation-induced acoustic cavitation; threshold versus temperature for some liquids. *J. Acoust. Soc. Am.*, 1982;72:1327–1331.

- Guan P, Lu S, Spector MJ, Valavala PK, Falk ML. Cavitation in amorphous solids. *Phys. Rev. Letters*, 2013;110:185502.
- Herbert E, Balibar S, Caupin F. Cavitation pressure in water. *Phys. Rev. E*, 2006;74:041603.
- Jin F, Li J, Ye X, Wu C. Effects of pH and ionic strength on the stability of nanobubbles in aqueous solutions of α -cyclodextrin. *J. Phys. Chem. B*, 2007;111:11745–11749.
- Kamath V, Prosperetti A, Egolfopoulos F. A theoretical study of sonoluminescence. *J. Acoust. Soc. Am.*, 1993;94:248–260.
- Keller JB, Miksis M. Bubble oscillations of large amplitude. *J. Acoust. Soc. Am.*, 1980;68:628–633.
- Khokhlova VA, Fowlkes JB, Roberts WW, Schade GR, Xu Z, Khokhlova TD, Hall TL, Maxwell AD, Wang YN, Cain CA. Histotripsy methods in mechanical disintegration of tissue: Towards clinical applications. *International journal of hyperthermia*, 2015;31:145–162.
- Leighton T. *The acoustic bubble*. Academic press, 2012.
- Mancia L, Vlasisavljević E, Xu Z, Johnsen E. Predicting tissue susceptibility to mechanical cavitation damage in therapeutic ultrasound. *Ultrasound Med. Biol.*, 2017;43:1421–1440.
- Mancia L, Vlasisavljević E, Yousefi N, Rodriguez M, Ziemlewicz TJ, Lee FT, Henann D, Franck C, Xu Z, Johnsen E. Modeling tissue-selective cavitation damage. *Phys. Med. Biol.*, 2019;64:225001.
- Maxwell AD, Cain CA, Hall TL, Fowlkes JB, Xu Z. Probability of cavitation for single ultrasound pulses applied to tissues and tissue-mimicking materials. *Ultrasound Med. Biol.*, 2013;39:449–465.
- Nirmalkar N, Pacek A, Barigou M. Interpreting the interfacial and colloidal stability of bulk nanobubbles. *Soft matter*, 2018a;14:9643–9656.
- Nirmalkar N, Pacek A, Barigou M. On the existence and stability of bulk nanobubbles. *Langmuir*, 2018b;34:10964–10973.

- Parsons JE, Cain CA, Abrams GD, Fowlkes JB. Pulsed cavitation ultrasound therapy for controlled tissue homogenization. *Ultrasound in medicine & biology*, 2006;32:115–129.
- Parsons JE, Cain CA, Fowlkes JB. Spatial variability in acoustic backscatter as an indicator of tissue homogenate production in pulsed cavitation ultrasound therapy. *IEEE transactions on ultrasonics, ferroelectrics, and frequency control*, 2007;54:576–590.
- Prosperetti A. The thermal behaviour of oscillating gas bubbles. *J. Fluid Mech.*, 1991;222:587–616.
- Prosperetti A, Crum LA, Commander KW. Nonlinear bubble dynamics. *J. Acoust. Soc. Am.*, 1988;83:502–514.
- Salzar RS, Treichler D, Wardlaw A, Weiss G, Goeller J. Experimental investigation of cavitation as a possible damage mechanism in blast-induced traumatic brain injury in post-mortem human subject heads. *J. Neurotrauma*, 2017;34:1589–1602.
- Sankin G, Teslenko V. Two-threshold cavitation regime. *Dokl. Phys.*, 2003;48:665–668.
- Shampine LF, Reichelt MW. The matlab ode suite. *SIAM J. Sci. Comput.*, 1997;18:1–22.
- Shampine LF, Reichelt MW, Kierzenka JA. Solving index-1 daes in matlab and simulink. *SIAM Rev.*, 1999;41:538–552.
- Singh I, Narasimhan R, Ramamurty U. Cavitation-induced fracture causes nanocorrugations in brittle metallic glasses. *Phys. Rev. Letters*, 2016;117:044302.
- Sukovich JR, Haskell SC, Xu Z, Hall TL. A cost-effective, multi-flash, ghost imaging technique for high temporal and spatial resolution imaging of cavitation using still-frame cameras. *The Journal of the Acoustical Society of America*, 2020;147:1339–1343.
- Uchida T, Liu S, Enari M, Oshita S, Yamazaki K, Gohara K. Effect of nacl on the lifetime of micro-and nanobubbles. *Nanomaterials*, 2016;6:31.

- Vlaisavljevich E, Lin KW, Maxwell A, Warnez MT, Mancina L, Singh R, Putnam AJ, Fowlkes B, Johnsen E, Cain C, et al. Effects of ultrasound frequency and tissue stiffness on the histotripsy intrinsic threshold for cavitation. *Ultrasound Med. Biol.*, 2015;41:1651–1667.
- Vlaisavljevich E, Maxwell A, Warnez M, Johnsen E, Cain C, Xu Z. Histotripsy-induced cavitation cloud initiation thresholds in tissues of different mechanical properties. *IEEE Trans. Ultrason. Ferroelectr. Freq. Control*, 2014;61:341–352.
- Vlaisavljevich E, Xu Z, Maxwell AD, Mancina L, Zhang X, Lin KW, Duryea AP, Sukovich JR, Hall TL, Johnsen E, et al. Effects of temperature on the histotripsy intrinsic threshold for cavitation. *IEEE Trans. Ultrason. Ferroelectr. Freq. Control*, 2016;63:1064–1077.
- Walton AJ, Reynolds GT. Sonoluminescence. *Adv. Phys.*, 1984;33:595–660.
- Wang YC. Effects of nuclei size distribution on the dynamics of a spherical cloud of cavitation bubbles. *J. Fluids Eng.*, 1999;121:881–886.
- Warnez M, Johnsen E. Numerical modeling of bubble dynamics in viscoelastic media with relaxation. *Phys. Fluids*, 2015;27:063103.
- Wienken W, Stiller J, Keller A. A method to predict cavitation inception using large-eddy simulation and its application to the flow past a square cylinder. *J. Fluids Eng.*, 2006;128:316–325.
- Wilkerson J, Ramesh K. Unraveling the anomalous grain size dependence of cavitation. *Phys. Rev. Letters*, 2016;117:215503.
- Wilson CT, Hall TL, Johnsen E, Mancina L, Rodriguez M, Lundt JE, Colonius T, Henann DL, Franck C, Xu Z, et al. Comparative study of the dynamics of laser and acoustically generated bubbles in viscoelastic media. *Phys. Rev. E*, 2019;99:043103.
- Xu Z, Fowlkes JB, Rothman ED, Levin AM, Cain CA. Controlled ultrasound tissue erosion: The role of dynamic interaction between insonation and microbubble activity. *The Journal of the Acoustical Society of America*, 2005;117:424–435.
- Zhu J, An H, Alheshibri M, Liu L, Terpstra PM, Liu G, Craig VS. Cleaning with bulk nanobubbles. *Langmuir*, 2016;32:11203–11211.